Experimental measurement of wall shear stress in strongly disrupted flows

E. Rodríguez-López[1], P.J.K. Bruce & O.R.H. Buxton
[1]:Corresponding author. Email: eduardo.rodriguez-lopez12@imperial.ac.uk
Department of Aeronautics.
Imperial College London.
Exhibition Road SW7 2AZ.
London, United Kingdom.

Abstract

Mean and fluctuating wall shear stress is measured in strongly disrupted cases generated by various low-porosity wall-mounted single- and multi-scale fences. These grids generate a highly turbulent wake which interacts with the wall-bounded flow modifying the wall shear stress properties. Measurement methods are validated first against a naturally growing zero pressure gradient turbulent boundary layer showing accuracies of 1% and 4% for extrapolation and direct measurement of the mean shear stress respectively. Uncertainty associated with the root mean square level of the fluctuations is better than 2% making it possible to measure small variations originating from the different fences. Additionally, probability density functions and spectra are also measured providing further insight into the flow physics. Measurement of shear stress in the disrupted cases (grid+TBL) suggest that the flow characteristics and turbulence mechanisms remain unaltered far from the grid even in the most disrupted cases. However, a different root mean square level of the fluctuations is found for different grids. Study of the probability density functions seem to imply that there are different degrees of interaction between the inner and outer regions of the flow.

1 Introduction

Measurement of wall shear stress has important implications in drag determination or flow characterization. Further, from a fundamental point of view, the scaling of lengths and velocities in a turbulent boundary layer (TBL) is dominated by the wall shear stress, τ_w; see, for instance, (Schlichting and Gersten, 2000). As such, several methods have been developed and tested to obtain its mean and instantaneous value; (see (Tropea and Yarin, 2007) for an exhaustive review of several experimental methods). For naturally growing zero pressure gradient (ZPG) TBL, several studies have focused on different properties of the wall shear stress such as: mean value (Nagib et al., 2004, 2007; Chauhan et al., 2009), root mean square (rms) level of the fluctuations (Schlatter and Örlü, 2010a), probability density function (Alfredsson et al., 2011), spectral content (Hu et al., 2006; Örlü and Schlatter, 2011) or convection velocity (in channels) (Jeon et al., 1999). This comprehensive collection of studies provides a solid base to rely upon in order to extend the knowledge of the shear stress behaviour to more complex cases such as the interaction of various obstacle's wakes and a TBL. Moreover, they can also be used to validate experimental methods or to develop new processing strategies.

Wall shear stress can also be employed as a diagnostic quantity to characterize the recovery of natural (canonical) TBL properties downstream of disturbances such as pressure gradient history or geometric obstacles (Chauhan et al., 2009; Marusic et al., 2015; Rodríguez-López et al., 2016a). Amongst others, these studies concluded that the wall shear stress and the near-wall turbulent structures recover more quickly than outer TBL regions from upstream disturbances. This effect has also been reported as a shorter 'memory' of the near-wall structures (Simens et al., 2009). Furthermore, Rodríguez-López et al. (2016a) hypothesised that there are two distinct methods (so-called wake- and wall-driven) by which a perturbed boundary layer recovers canonical properties: short adaptation regions are associated with a wall-driven mechanism in which turbulent structures near the wall recover quickly. This is in contrast to the wake-driven mechanism, where the strong influence of an obstacle's wake disrupts the flow in the near-wall region to a larger extent, making it harder for canonical TBL properties to be recovered.

The main objective of this paper will be to characterize the behaviour of the wall shear stress downstream of various wall-mounted porous fences and to relate its properties to the turbulence generated by those fences. Additionally, the recovery of canonical properties regarding the wall shear stress will be presented, showing that

different grids need clearly distinct adaptation lengths for the wall shear stress to adapt from a disrupted case to a more canonical form.

In order to pursue these objectives, a comprehensive study of the wall-shear stress is conducted including direct and indirect measurements of the mean and instantaneous wall shear stress. Two main experimental approaches are employed: extrapolation of $u_\tau = \sqrt{\overline{\tau_w}/\rho}$ ($\overline{\tau_w}$ is the mean wall shear stress and ρ is the fluid density) from the velocity profile, and measurements based on heat transfer (wall-mounted hot wire). Regarding the extrapolation methods, the classical approach of Clauser (1954) has been refined over the years to improve its accuracy and allow the determination of the wall-probe relative position (Kendall and Koochesfahani, 2008; Rodríguez-López et al., 2015; Vinuesa and Nagib, 2016). However, these methods only facilitate measurements of the mean value of τ_w. On the other hand, constant temperature anemometry enables the instantaneous value of the wall shear stress to be determined. Due to their large thermal inertia, hot films present a damping of the fluctuations in low thermal conductivity fluids (as first reported by Alfredsson et al., 1988); hence a wall-mounted hot wire will be employed due to its better frequency response.

The current approach will be to disrupt the boundary layer with porous wall-mounted fences generating a highly turbulent flow close to the wall. Single- and multiscale grids[1] have been deeply studied in the last years. Many researchers including (Hurst and Vassilicos, 2007; Laizet and Vassilicos, 2009; Mazellier and Vassilicos, 2010; Suzuki et al., 2010; Valente and Vassilicos, 2011, 2012; Gomes-Fernandes et al., 2012; Discetti et al., 2013) have tested a range of so-called fractal grids based on three different patterns and have demonstrated the existence of new scalings to describe the evolution of turbulence intensity downstream of regular and multiscale grids. Similar multiscale geometries have been applied to several practical applications relating to noise of aerodynamic spoilers (Nedić et al., 2012), study of wakes (Nedić et al., 2013; Dairay et al., 2015), aerodynamic performance (Nedić and Vassilicos, 2015), combustion mixing (Goh et al., 2013, 2014) or vortex shedding study (Nedić et al., 2015; Melina et al., 2016). Special mention is required for Keylock et al. (2012) who tested multiscale grids in the pressence of a TBL. However, their various multiscale patterns were obtained by changing spacing and thickness of horizontal bars only hence generating a different kind of flow than in the present study. Furthermore, their frontal blockage ratio was also significantly larger, making the comparisons with the present experiment almost impossible. Thus, the interaction of multiscale generated turbulence with a TBL remains an open question and this paper will try to quantify the influence that different grids have on the near-wall turbulence mechanisms.

To summarize, recent studies (Schlatter and Örlü, 2012; Marusic et al., 2015; Rodríguez-López et al., 2016a,b) have shown that the recovery of canonical properties might be associated with the interaction between wake and near-wall regions. Consequently, in order to study this effect, several disruptions in which a large energetic wake are designed to this purpose. Given the potential and possible applications of multiscale geometries, various patterns based on this idea are tested to assess their different behaviours. This assessment will be performed as a function of the wall shear stress because of its faster recovery after severe disruptions (Simens et al., 2009; Schlatter and Örlü, 2012) and also because of its fundamental implications on the scalings within a TBL.

The structure of the paper is as follows: Section 2 will describe the experimental set-up (wind tunnel, grids and sensors) employed. A validation of the different methods will be presented in section 3 for the natural (without grid) case. Section 4 will present the results of the shear stress for the disrupted cases (TBL + grid) and section 5 will draw the main conclusions of the study.

2 Experimental set-up

2.1 The wind tunnel

Experiments were conducted at Imperial College London in a wind tunnel of $0.91 \times 0.91\,\mathrm{m}^2$ section and 4.8 m length, with freestream velocity $U_e = 10\,\mathrm{m\,s^{-1}}$. At these conditions, the incoming freestream turbulence level is $\lesssim 0.05\%$. The same wind tunnel has been broadly documented before (e.g. Mazellier and Vassilicos, 2010; Valente and Vassilicos, 2014; Rodríguez-López et al., 2016a).

A wooden flat plate of thickness 16 mm is mounted vertically spanning the whole wind tunnel with an elliptic (10 : 1) leading edge to avoid separation, and a trailing edge flap in order to modify the position of the stagnation point on the leading edge and control the pressure gradient along the plate. A strip of sand paper 20 mm long is placed at $x = 80$ mm (immediately following the elliptic leading edge) to ensure transition to a TBL. A sketch of the set-up can be seen in figure 1(a); similar experimental arrangement was used in (Rodríguez-López et al., 2016a). The pressure gradient is shown in Fig. 1(b); the strongly positive pressure gradient present in the last part of the plate for both configurations is due to the presence of the flap. Although a slightly favourable pressure gradient was present in the central part of the plate, results in terms of mean and fluctuating wall shear stress show a good agreement with canonical zero pressure gradient (ZPG) TBL trends (as will be shown below). The different grids were all located at $x = 100$ mm where the thickness of

[1] For readability, the terms grid or porous fence will be used equivalently throughout this paper

the boundary layer is negligible with respect to the height of the grid. The coordinate system defines x as the streamwise distance downstream of the plate leading edge, y as the wall-normal distance from the plate, and z as the spanwise distance relative to the centreline. Mean quantities will be denoted by a horizontal bar while the fluctuating part is shown with a superscript $'$ (e.g. $a(t) = \bar{a} + a'(t)$). The superscript $+$ is used for magnitudes expressed in wall units, i.e. non-dimensionalized with the viscosity, ν, and the friction velocity, u_τ. In particular a wall unit is defined as $\delta_\nu = \nu/u_\tau$, thus $y^+ = y/\delta_\nu$, $u^+ = u/u_\tau$ and the frequency, $f^+ = f\nu/u_\tau^2$.

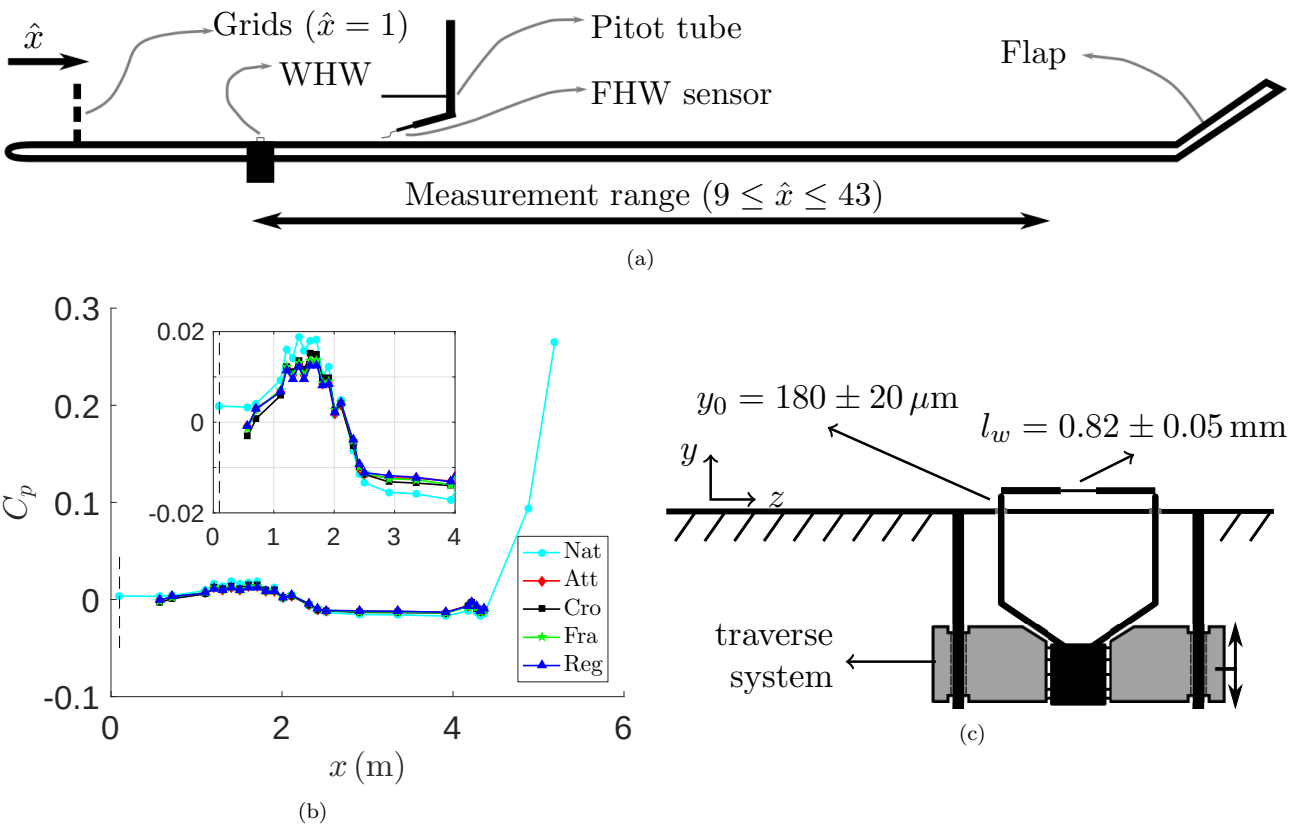

Figure 1: (a) Sketch of the flat plate, grid and sensors location. (b) Pressure gradient along the flat plate for different configurations with or without grid (described in section 2.3). Dashed black line shows the location at which the grids were installed. (c) Sketch of the wall hot wire (WHW) sensor.

2.2 The sensors

Two different anemometers are employed in order to measure mean and fluctuating shear stress by different means:

Velocity profiles are acquired with an in-house etched hot wire soldered on the prongs of a 55P05 Dantec Dynamics sensor. It is operated in constant temperature mode with an overheat ratio of $OHR = 1.8$. The sensing part is made of wollaston wire yielding a final diameter $d_w = 5\,\mu$m and a length $l_w \approx 1$ mm. This length provides a compromise between keeping the aspect ratio of the hot wire l_w/d_w above 200 while minimising any attenuation of the large wave-numbers due to insufficient spanwise resolution. For the various flow configurations the resolution in inner units ranged from $l_w^+ \approx 15$ to $l_w^+ \approx 25$. The hot-wire is placed in the near wall region with the help of a microscope allowing the first measurement point to be located well below 10 wall units. However, the accurate initial position y_0^+ is later determined from the velocity profile as will be described in section 3.1. This sensor will be called FHW (Free Hot Wire) for brevity.

A second sensor was built by attaching the body of a 55P01 Dantec Dynamics hot wire to a linear traverse mounted on the back of the flat plate. The two tips of the prongs were passed through two holes which were then sealed with wax to avoid any leakage flow. The sensor is built with a $d_w = 5\,\mu$m wollaston wire etched to a length of $l_w = 0.82 \pm 0.05$ mm and operated with an overheat ratio of $OHR = 1.8$. The value of $l_w/d_w \approx 164$ is slightly lower than the recommended value of 200 hence a correction to this effect may be applied (Hultmark et al., 2011; Miller et al., 2014). However, this correction only marginally modifies the measured value as will be shown in section 3.2. The linear traverse enabled positioning of the hot wire in close vicinity to the wall while minimizing conductive heat loss to it. By keeping the position constant (in physical units) and equal to

$y_0 = 180 \pm 20\,\mu$m it was possible for these effects to be calibrated out. A sketch of the mounting along with the most significant dimensions is shown in figure 1(c). This sensor will be called WHW (Wall Hot Wire) for brevity.

Note that none of the sensors allow for the characterization of flow reversals close to the wall. However, these negative velocity events are reported to happen only about 0.06% of the time for a natural TBL at $Re_\tau = 1000$ (Lenaers et al., 2012). Furthermore, they also reported that the ability to detect these events decays drastically with the spanwise resolution, l_w. Hence the potential bias introduced in the statistics is expected to be significantly smaller than any other source of experimental uncertainty (such as l_w^+ or l_w/d_w effects which will be accounted for in section 3.2). Despite the flow disruption generated by the grids, the proportion of flow reversal incidents is also expected to be small in the disturbed cases.

FWH sensor is statically calibrated against a straight Pitot and the points are fitted by King's Law. In order to adequately calibrate the wall shear stress sensor, one must accurately know the shear stress for a range of different freestream velocities. For that, several velocity profiles ($2 \leq U_e \leq 16\,\mathrm{ms}^{-1}$ in steps of $2\,\mathrm{ms}^{-1}$) are taken (without grid) at the furthest streamwise position ($x = 4270\,$mm) and the wall shear stress is extrapolated according to the method described in (Rodríguez-López et al., 2015). This method fits a canonical description of the boundary layer to the experimental data and has been shown to yield an accuracy better than 1% in the determination of the friction velocity u_τ even in moderately disrupted cases. Hence its accuracy is deemed sufficient for the current purposes. Other methods of extrapolation based on the mean profile were also tested and the differences were within the experimental uncertainty (details will be given in section 3.1).

The WHW response was fitted to the values of known (extrapolated from velocity profiles) shear stress. King's Law and a 4th order polynomial fits were tried; slightly better fit was obtained with the polynomial therefore that method was employed for the calculations. In any case results were qualitatively independent of the fitting method employed.

2.3 The grids

Four different porous fences are designed and mounted. All of them span 88% of the flat plate with a height h of 100 mm. Magnitudes marked with a hat, $\wedge$, are non-dimensionalized with the grid's height, $\hat{y} = y/h$, $\hat{x} = x/h$. The final spanwise extent is obtained by the periodic repetition of the basic patterns described below; all the grids have the same blockage ratio $\sigma = 30\%$. The grids were mounted normal to the flat plate at $x = 0.1\,$m by means of thin legs (threaded rods of 3 mm diameter) which passed to the rear side of the plate where they were held by a nut. At least four legs were used per grid in order to keep them solidly attached to the plate at a constant angle. Figure 2.3 shows the drawing of the grids' basic pattern. The name *Nat* will be used to refer to the natural configuration (without any grid mounted).

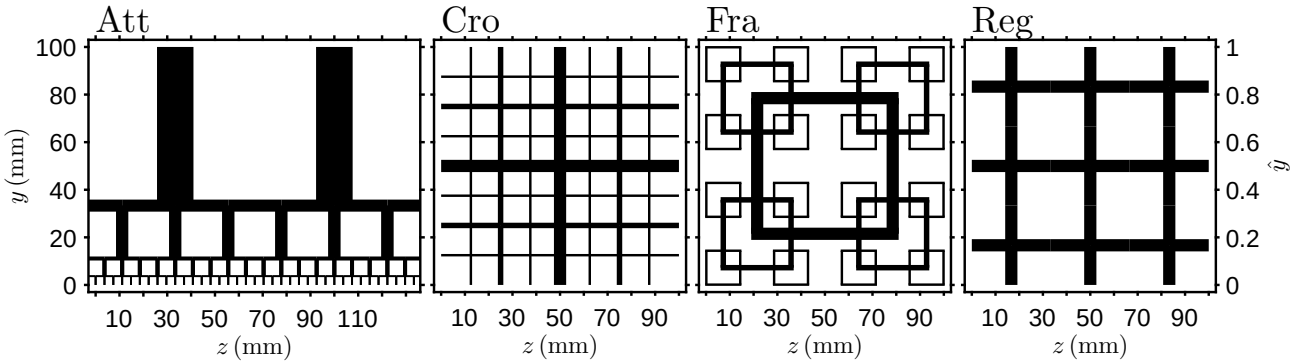

Figure 2: Drawings of the basic pattern of the four tested grids. Note that thickness and length of the bars is to scale within the pictures.

Att. This grid was obtained based on the attached eddy hypothesis of Townsend (1976); to that regard, eddy size would scale with its distance from the wall. The grid was designed stacking four squares with lengths l_i $i = 0, \ldots, 3$, where l_i equals the distance from their centre to the wall. This produces a geometric distribution of squares with sizes up to fill the grid height of 100 mm. The upper most bar was removed from the design in order to avoid a large blockage in the outer region of the flow which would be significantly at odds with the other designs and not representative of a TBL. In order to appropriately scale the bar thickness, t_i this is kept as a constant fraction ($l_i/t_i = 4.51$) of the squares' length throughout the four iterations.

Cro. The grid design is based on a fractal cross pattern first described by Hurst and Vassilicos (2007). The only free parameters to fix are the number of iterations (which was kept to 3 due to the impossibility of manufacturing bars of smaller thickness); the thickness of the largest bar $t_0 = 5.6\,$mm and the thickness ratio

$t_r = t_0/t_2 = 5$ (relation of the largest and smallest thickness). This grid has also been employed as a turbulence generator for combustion of opposed jets Goh et al. (2013, 2014).

Fra. The grid design is based on the fractal square pattern described by Hurst and Vassilicos (2007). The number of iterations, 3, and thickness ratio ($t_r = 5$) are chosen to be the same as the *Cro* case and the thickness of the largest bar as similar as possible ($t_0 = 5\,\text{mm}$). This parameter cannot be varied independently from the blockage ratio which has to be $\sigma = 30\%$ for every grid. Turbulent properties of this grid have been extensively studied in the past years (e.g Hurst and Vassilicos, 2007; Laizet and Vassilicos, 2012; Valente and Vassilicos, 2014; Melina et al., 2016, amongst others).

Reg. In order to characterize the effect of different bars arrangements; a regular grid is designed matching the same blockage ($\sigma = 30\%$) and thickness ($t = 5\,\text{mm}$) of the multiscale cases.

3 Methodology and validation

Before analysing the results of the shear stress under the influence of different porous fences; we present the followed methodology in a detailed manner. Results for several aspects of τ_w (mean, rms, probability density function, spectra) will be presented for the natural ZPG TBL case (without any porous fence) and compared with the trends appearing in the literature for turbulent boundary layers. In particular mean shear stress (directly measured and extrapolated from the velocity profile) will be compared with the relationship given in (Chauhan et al., 2009); rms level of the fluctuations with the correlation proposed in (Schlatter and Örlü, 2010a) and probability density function and spectra with (Örlü and Schlatter, 2011; Alfredsson et al., 2011). This validation aims to set the basis for the experimental setting and methodology that will be employed later on for the characterization of the disrupted cases (grid+TBL).

Several studies in the past few years have shown that downstream of strong disturbances the TBL evolves towards canonical properties after an adaptation region (Schlatter and Örlü, 2012; Marusic et al., 2015; Rodríguez-López et al., 2016a,b). They have also shown that quantities related with the inner layer of the TBL (such as $\overline{\tau_w}$, $\tau^{\prime+}_{w,rms}$, etc. considered here) are expected to present a shorter adaptation region than outer properties (such as the mean velocity profile or the shape factor). Thus, it seems reasonable to assume (as it will be confirmed in section 4) that the validation of the measurement methodology in a natural TBL suffices in order to assess the uncertainty of the same methodology (WHW measurements) applied to the flow downstream of porous fences.

3.1 Mean shear stress $\overline{\tau_w}$

Extrapolation of the mean wall shear stress from the velocity profile can provide accurate results in canonical or mildly disrupted boundary layers as mentioned above. However, the use of these kind of methods is challenging in the present case where the flow is strongly disrupted by the presence of the porous fences and therefore the mean velocity profile does not resemble the standard ZPG TBL shape. A first stage is dedicated to the comparison between various methods of extrapolation and the direct measurement of the shear stress in a natural TBL in order to assess their validity. An additional difficulty is introduced by the fact that the initial probe-wall relative position is not known *a priori* and hence has to be extrapolated from the mean velocity profile. Four methods available in the literature are used and briefly described below:

RBB15 (Rodríguez-López et al., 2015). This method compares the experimental velocity profile with the canonical description given by the composite profile of Chauhan et al. (2009). The composite profile is taken as a function of five parameters, $\{u_\tau, \Delta y, \kappa, \delta, \Pi\}$, where Δy allows for an offset on the wall-probe initial position, κ is the von Kármán constant (which is also extrapolated from the velocity profile, not treated as a constant), δ is the thickness of the boundary layer and Π is the wake parameter. The quoted uncertainty of the method is $< 1\%$ in the determination of u_τ for perfectly accurate velocity measurements; it may be expected to be larger given the uncertainty associated to the velocity profile itself.

VN16 (Vinuesa and Nagib, 2016). The method was originally developed and tested to extrapolate the wall-probe relative position *for a known* u_τ. In the present study we have extended the method to simultaneously extrapolate Δy and u_τ. The method has two steps, first for a given pair $\{u_\tau, \Delta y\}$, a Musker (1979) profile is fitted to the velocity profile for $y < 0.1\delta$ in order to obtain κ and B (the linear intercept of the logarithmic layer). The residual of the method is found as the distance between the pair $\{\kappa, B\}$ and the curve $\kappa B = 1.6\,[\exp 0.1663B - 1]$ first proposed by Nagib and Chauhan (2008). The final solution is the pair $\{u_\tau, \Delta y\}$ which minimizes that distance. According to Vinuesa and Nagib (2016) the method out-performed others based on composite profiles when determining Δy alone; but it was not tested for u_τ hence no uncertainty is quoted.

KK08 (Kendall and Koochesfahani, 2008). This method proposes a fit of the Musker (1979) velocity profile (with a fixed $\kappa = 0.384$) to the inner region in order to obtain the pair $\{u_\tau, \Delta y\}$ which minimizes the residual between the data and the Musker (1979) description. A sensitivity analysis to the upper limit of the fitting is presented in their paper concluding that the sensitivity is very small with a correct definition of the residual

(giving a preferential weight to points closer to the wall); the value of $y < 0.1\delta$ is adopted here for consistency with the VN16 method.

AOS11 (Alfredsson et al., 2011). Contrasting with the previous three methods, this does not use the mean velocity profile but, on the contrary, the self-similarity of the cumulative density function of the fluctuations, CDF(u') in the inner region of the TBL ($y^+ < 7$). Despite being promising, the method requires the prescription of a large number of parameters (region of the flow to consider, $y^+ < 7$; number of points to eliminate due to extra heat conduction to the wall, explained in section 3.2; part of the CDF to consider as self similar, $0.1 \leq CDF(u') \leq 0.6$; etc.). Furthermore, it assumes as universal a log-normal distribution with mean -0.08 and standard deviation 0.42, whereas hot-wire experiments may suffer from a reduced variation due to the spanwise filter imposed by their finite resolution. It also allows determination of the relative wall-probe position.

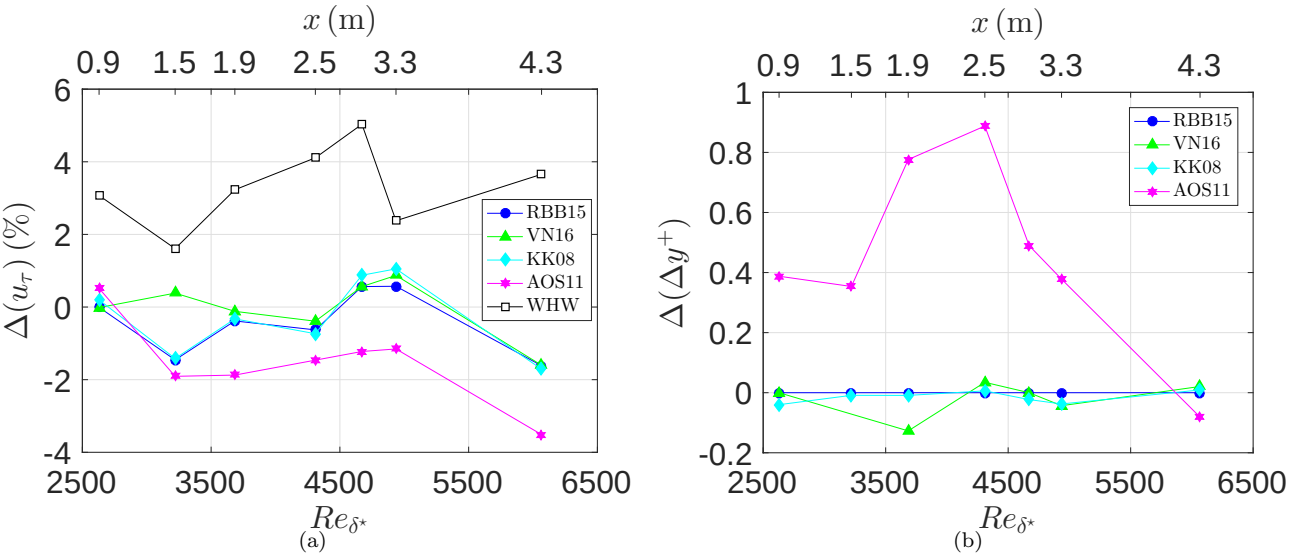

Figure 3: (a) Performance of the different methods to obtain u_τ extrapolated from the velocity profile (filled symbols) and directly measured (empty symbols). Equation 1 is taken as the reference case as in Chauhan et al. (2009). (b) Comparison of the wall-probe relative position for different extrapolation methods (RBB15 is taken as the reference case).

Figure 3 shows the performance of the four aforementioned extrapolation methods along with the results of the WHW sensor, described in section 2. In order to check the performance of an arbitrary method j we define $\Delta u_\tau^j = (u_\tau^{CMN09} - u_\tau^j)/u_\tau^{CMN09}$, where u_τ^{CMN09} is given as the extended Coles-Fernholz skin friction relation (Nagib et al., 2007; Chauhan et al., 2009):

$$u_\tau^{CMN09} = U_e \left[\frac{1}{\kappa} ln(Re_{\delta^\star}) + C + \frac{D_0 ln(Re_{\delta^\star})}{Re_{\delta^\star}} + \frac{D_1}{Re_{\delta^\star}} \right]^{-1} ; \tag{1}$$

with $C = 3.3$, $D_0 = 182$, $D_1 = -2466$ and $Re_{\delta^\star} = \delta^\star U_e/\nu$ is the Reynolds number based on the displacement thickness. Given that the true solution for the wall-probe relative position is not known, the results are compared with the extrapolation performed by RBB15 method in order to show the relative differences between methods, consequently for a given method j we define $\Delta(\Delta y^+)_j = \Delta y_j^+ - \Delta y_{RBB15}^+$.

Two observations regarding the performance of the different methods can be made at this point: first, while the three methods based on the comparison with a mean profile (RBB15, VN16 and KK08) present virtually the same, smallest level of uncertainty, the method based on the fluctuating part (AOS11) presents a slightly larger uncertainty (especially in the determination of Δy). However, all the extrapolation methods show good accuracy with an uncertainty that can be assumed to be $\mathcal{O}(1\%)$ for u_τ and $\mathcal{O}(0.5\delta_\nu)$ for Δy^+. Secondly, the performance of the direct sensor is slightly worse in terms of u_τ determination. Moreover, it seems that WHW sensor tends to overestimate u_τ by about 3%. This greater uncertainty is not surprising given the larger variation that the points of the calibration may present because of being extrapolated from the velocity profile. Nevertheless, one can quote an associated uncertainty of $\mathcal{O}(4\%)$ for this method which, despite higher than the extrapolations, is still reasonable for a direct measurement of u_τ; moreover in strongly disrupted flows where the extrapolation from the velocity profile is no longer possible due to strong departure from the canonical case.

3.2 Fluctuating shear stress $\tau_{w,rms}^{\prime +}$

Due to the limited spanwise resolution of wall-mounted hot wires such as the one employed here, there is an artificial attenuation of the fluctuations caused by the inability of the probe to resolve eddies smaller than l_w^+.

This effect has been widely reported and several corrections are available in the literature to account for it (e.g. Chauhan et al., 2009; Smits et al., 2011; Segalini et al., 2010; Talamelli et al., 2013, , amongst others). However, several of these corrections are aimed to improve the accuracy of the turbulence intensity peak ($y^+ \approx 15$) rather than the fluctuating wall shear stress. Noting the definition of shear stress and assuming $u^+ = y^+$ for $y \to 0$ it can be shown

$$\frac{\tau'_{w,rms}}{\overline{\tau_w}} = \lim_{y^+ \to 0} \frac{u'_{rms}}{\overline{u}}\,, \tag{2}$$

and considering a correction scheme of the form $\overline{u'^2}^+|_{true} = C_1(l_w^+, y^+)C_2(l_w/d_w, y^+)\overline{u'^2}^+|_{raw}$; the correction applied to the fluctuating wall shear stress would be $\tau'^+_{w,rms}|_{true} = \sqrt{C_1(l_w^+, y^+ = 0)C_2(l_w/d_w, y^+ = 0)}\tau'^+_{w,rms}|_{raw}$. In this study the correction scheme proposed by Smits et al. (2011) will be used to account for the spanwise filtering effects. This scheme is based on the attached eddy hypothesis and takes the form $C_1(l_w^+, y^+) = [1 + M(l_w^+)g(y^+)]$. The correction proposed by Miller et al. (2014) based on the Γ parameter defined by Hultmark et al. (2011) will be employed for the end-conduction effects as $C_2(l_w/d_w, y^+ = 0) = [1 - g(y^+ = 0)20(\Gamma + 2.7)^{-2.2}\overline{u^+}/\overline{u^+}_{15}]^{-1}$, where $\overline{u^+}_{15} = 12$ is the mean velocity at $y^+ = 15$, $\overline{u^+} = 3$ is the mean velocity at the measurement point,

$$M(l_w^+) = 0.0091 l_w^+ - 0.069, \tag{3a}$$

$$g(y^+ = 0) = \left.\frac{15 + \log(2)}{y^+ + \log(\exp(15 - y^+) + 1)}\right|_{y^+=0} = 1.0462\,, \tag{3b}$$

$$\Gamma = \frac{l_w}{d_w}\sqrt{\frac{4 \cdot OHR \cdot Nu \cdot k_f}{k_w}} = 11.8\,. \tag{3c}$$

Where $Nu = (0.35 + 0.56 Re_w^{0.52})Pr^{0.3} = 1.23$ is the Nuselt number for Reynolds number based on the wire diameter $Re_w = 3.18$ and Prandtl number $Pr = 0.7$ (Fand, 1965), $k_w = 71.6\,\mathrm{Wm^{-1}K^{-1}}$ is the heat conductivity for platinum wires and $k_f = 0.042\,\mathrm{Wm^{-1}K^{-1}}$ is the heat conductivity for air at the wire temperature.

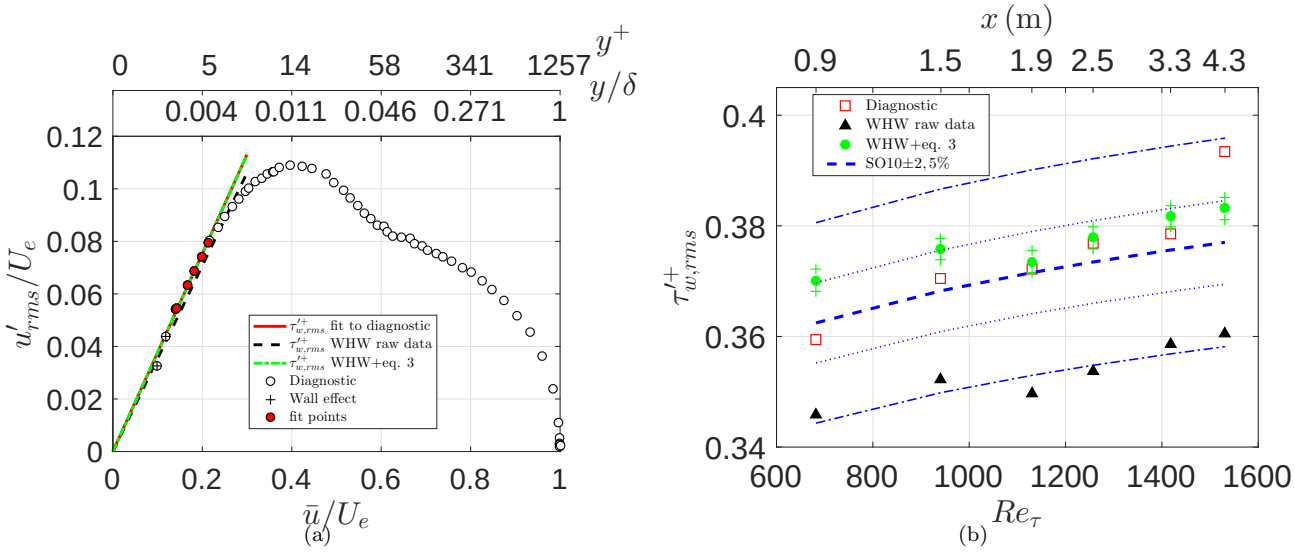

Figure 4: (a) Diagnostic plot (empty circles) showing also discarded points (with crosses) and points in the linear region (filled) employed to fit a straight line from the origin (solid line). Dot-dashed and dashed line show the value of $\tau'^+_{w,rms}$ measured with WHW sensor with and without correction respectively. (b) Dashed line –SO10– shows the correlation $\tau'^+_{w,rms} = 0.245 + 0.018\log(Re_\tau)$ (Schlatter and Örlü, 2010a) with ±2% (dotted) and ±5% (dot-dashed) margins. Solid triangles show the raw WHW data. Empty squares show $\tau'^+_{w,rms}$ computed from the slope in (a) (red solid line). Filled circles show WHW data corrected according to Smits et al. (2011) and Miller et al. (2014) (eq 3) and crosses mark the uncertainty in determining l_w^+ of WHW.

A further limitation has to be considered if $\tau'^+_{w,rms}$ is to be measured with common hot wires (FHW) applying the definition of equation 2. Points close enough to the wall are affected by heat conduction towards the wall which wrongly influence the determination of $\overline{u}$. This effect is usually reported to be confined below approximately $y^+ = 3.5$ (e.g. Krishnamoorthy et al., 1985; Chew et al., 1998; Hutchins and Choi, 2002). On the other hand, points further from the wall ($y^+ \gtrsim 5$) depart from linearity and equation 2 does not hold any more. A compromise approach can be the use of the diagnostic plot (Alfredsson and Örlü, 2010) as shown in figure 4(a) in order to (i) remove the points affected by the wall-effect and (ii) fit a straight line of the form $u'_{rms} = k\overline{u}$ to the points located $y^+ \leq 5$ unaffected by the wall-effect in such a way that the slope of that line, k,

would be the measured value of $\tau'^{+}_{w,rms}$ according to equation 2. A note of caution is needed regarding selection of the points affected by wall-effect; they depart from the linear trend but there is a certain subjectivity implied in the determination of this departure. Several criteria were tested including removing a larger (conservative) or smaller number of points and the results did not differ qualitatively. Note that this approach was applied *prior* to the extrapolation of u_τ described in section 3.1 and the points contaminated by the wall effect were not considered in any of the aforementioned methods.

Figure 4(b) shows the results of the fluctuating wall shear stress measured with the wall hot wire (WHW sensor) both uncorrected and using the correction given by Smits et al. (2011) and Miller et al. (2014) (equation 3). Results are compared with the correlation $\tau'^{+}_{w,rms} = 0.245 + 0.018\log(Re_\tau)$ provided by Schlatter and Örlü (2010a) based on DNS data (exempt from limited resolution effects) and with the value of $\tau'^{+}_{w,rms}$ extrapolated from the diagnostic plot as described above. Overall, an agreement better than 2% is obtained for every Reynolds number using the corrected data. The largest sources of uncertainty were the determination of the sensing length of the hot wire for the WHW data and the limited amount of points in the range $3.5 \leq y^+ \leq 5$ for the extrapolation from the diagnostic plot (this effect being especially relevant for the highest Re_τ value). Note that, although the data presented in figure 4(a) (acquired with the FHW sensor) also suffers from limited spanwise resolution, results are in good agreement with the proposed trend. This appears to justify the employment of a value of 0.42 for the standard deviation in the determination of u_τ by the AOS11 method (section 3.1), at least from a qualitative perspective.

3.3 Probability density function $F(\tau_w^+)$ and spectra $E_{11}(\tau_w^+)$

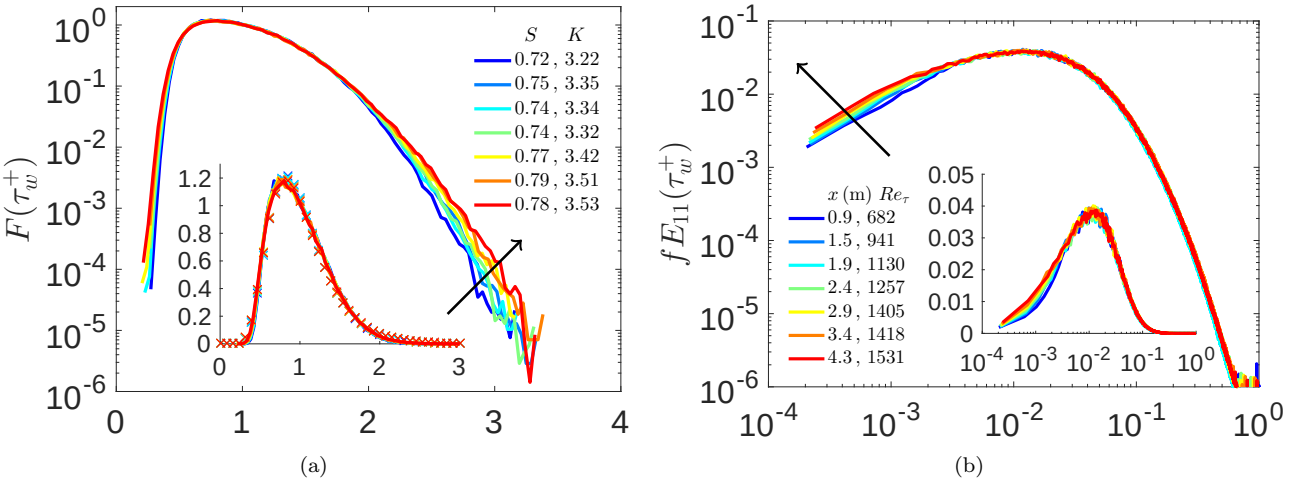

Figure 5: (a) Probability density function, $F(\tau_w^+)$. Arrow points in increasing Re_τ or, equivalently, increasing x, direction (given in legend of (b)). Crosses show log-normal distributions fitted to the data. Legend shows the values of kurtosis, K, and skewness, S, factors of the distributions. (b) Pre-multiplied power spectral density, $fE_{11}(\tau_w^+)$. Legend gives the values of x and Re_τ for each curve which is common for both sub-figures.

The final aspect of the validation of our wall shear stress measurements is the ability to reproduce probability density function (PDF) and spectral content of the fluctuations; we present these results in this section for the canonical TBL. Figure 5(a) shows the PDF of the wall shear stress for various streamwise locations (or analogously Re). Inner scaling is shown to adequately collapse the curves except for very extreme positive events. These occurrences present an increasing trend with Re (increasing in the arrow direction). Furthermore, the agreement with a log-normal distribution is also accurate as shown in the inset. These results are in a good agreement with those by (Örlü and Schlatter, 2011; Alfredsson et al., 2011). However, the existence of negative shear stress events cannot be distinguished with hot wires, hence no further assessment can be made to that effect. The values of higher order moments are also shown in figure 5(a); their value being smaller than those commonly reported in the literature ($S \approx 1$ and $K \approx 4.8$ by (Alfredsson et al., 1988)) probably due to wire-resolution effects (Talamelli et al., 2013).

The pre-multiplied spectral content of the fluctuations also shows a reasonable collapse in inner units except for small frequencies. This is probably due to the effect of the footprint that large structures resident in the logarithmic layer have on the wall (Mathis et al., 2009; Marusic et al., 2010a; Chernyshenko et al., 2012; Schlatter and Örlü, 2010b).

3.4 Summary of methodology

Several methods for extrapolation of u_τ and wall-probe relative position are tested in this section. Moreover, this is the first attempt (to the authors' knowledge) to use the method proposed by Alfredsson et al. (2011) to obtain u_τ and Δy. Additionally, further development to the method of Vinuesa and Nagib (2016) is successfully tested such that it can also extrapolate u_τ. All methods seem to provide consistent results of u_τ to within $\approx 1\%$ for extrapolated values and $\approx 4\%$ for direct measurements. For brevity, only results extrapolated with the method by Rodríguez-López et al. (2015) will be presented for the various grid flows.

Considering the value of the fluctuations, the proposed methodology (WHW data + Smits et al. (2011) Miller et al. (2014) corrections) agrees better than 2% with the correlation proposed by Schlatter and Örlü (2010a) based on DNS and without resolution effects. Furthermore, we present here an extra interpretation of the diagnostic plot to extrapolate $\tau^{\prime +}_{w,rms}$ from the velocity profile which seems to be less affected by spatial resolution effects. Probability density functions and spectra of τ_w unequivocally support inner scaling except for the influence of the large and very large structures on the wall which may be attributed to a Re effect.

4 Results

In the close vicinity of the porous fences the wall shear stress is dominated more by the grid's wake than the boundary layer mechanisms. However, this effect is expected to be less important further downstream. The inner region of the boundary layer, and more importantly, the wall shear stress recovers standard TBL properties faster than outer regions (Rodríguez-López et al., 2016a); this effect has been also reported as a shorter memory of inner scales (e.g. Simens et al., 2009; Chauhan et al., 2009, amongst others). Results will be presented regarding the mean and rms values, probability density function, spectra and autocorrelation or wall shear stress.

4.1 Mean shear stress $\overline{\tau_w}$

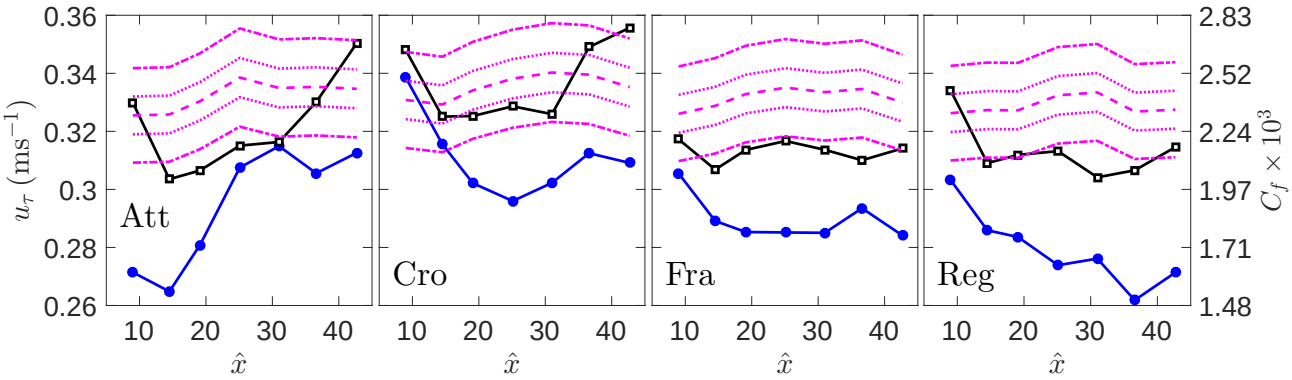

Figure 6: Mean friction velocity, u_τ, and friction coefficient, C_f, for various grids and streamwise locations. Solid blue circles are values extrapolated from the velocity profile with RBB15 method. Empty black squares show the direct measurement of shear stress with the WHW sensor. Pink dashed line is the value of u_τ according to Chauhan et al. (2009) (equation 1) ± 2, 5% (dotted and dashed-dotted lines respectively).

Mean wall shear stress for the different grids is presented in figure 4.1. Results are shown compared with the value of u_τ given by equation 1 (Chauhan et al., 2009) as a function of $Re_{\delta^\star}$. In the close vicinity of the grids, the velocity profile may not be monotonically increasing with the wall normal distance (as a consequence of wakes of large bars). This may represent a problem when integrating the velocity profile to obtain the displacement thickness. This effect is most pronounced for certain grids (*Cro* and *Reg*) and only in the first two streamwise locations (figure 7(a)). Direct measurement of the shear stress, u_τ^{WHW}, seems to provide results in reasonable agreement with the values proposed by Chauhan et al. (2009). However, extrapolation of u_τ^{RBB15} from the velocity profile seems to present a larger dispersion and a tendency for smaller values. Figure 3(a) showed that the results from WHW may overestimate the mean value by about 3%, this departure is larger for most of the cases than the difference between u_τ^{WHW} and u_τ^{RBB15}. Therefore it seems reasonable to assume that there is an artificial tendency for underestimation of the extrapolated value u_τ^{RBB15}. This result is not surprising given the clear departure of the velocity profiles from the canonical ZPG TBL case , figure 7, where, for brevity, mean velocity profiles are only shown at the closest location to the grid, $\hat{x} = 9$.

Note that, strictly speaking, RBB15 method should not be applied to the present flow (which far from resembles a canonical TBL). On the other hand, Rodríguez-López et al. (2015) showed that the method accurately recovered the correct values of u_τ even in moderately disrupted cases (pressure gradients, inner layer disruptions, etc.) therefore suggesting that there may be potential for this method to be applied in situations where, as in the present case, its main hypotheses do not hold. In any case, direct measurements, free from any hypothesis on the TBL state (u_τ^{WHW}), should be taken as true (once the validation in section 3.1 is considered). However, u_τ^{RBB15} is surprisingly close to capturing the overall trends of u_τ^{WHW}. Moreover, their difference is, for most of the cases, better than $\approx 10\%$. This result shows that, contrary to what it was assumed beforehand, the RBB15 method may provide some useful information about the flow in the absence of a direct determination of u_τ.

Assuming that, as shown in section 3.1, uncertainty associated with WHW sensor is $\mathcal{O}(4\%)$; even in the more disrupted cases, the value of u_τ^{WHW} is within $\approx 6\%$ of expected values for a canonical TBL. Note that this is true even in the close vicinity of the grids ($\hat{x} = 9$) where the velocity profile does not resemble a TBL. The most reasonable assumption is that, as shown in (Simens et al., 2009; Chauhan et al., 2009; Rodríguez-López et al., 2016a), small scales near the wall recover faster than in the outer region, at least for the mean value.

Summarizing, for the present measurements ($9 < \hat{x} < 43$) no matter how close to the grids we are ($\hat{x} = 9$) the mean wall shear stress will resemble (within the measurement uncertainty) the correspondent u_τ for equivalent $Re_{\delta^\star}$. This being true, it might imply that the fluctuations (which present a smaller uncertainty) would also tend to expected values; these results will be studied in the section 4.2 below.

4.2 Fluctuating shear stress $\tau'^{+}_{w,rms}$

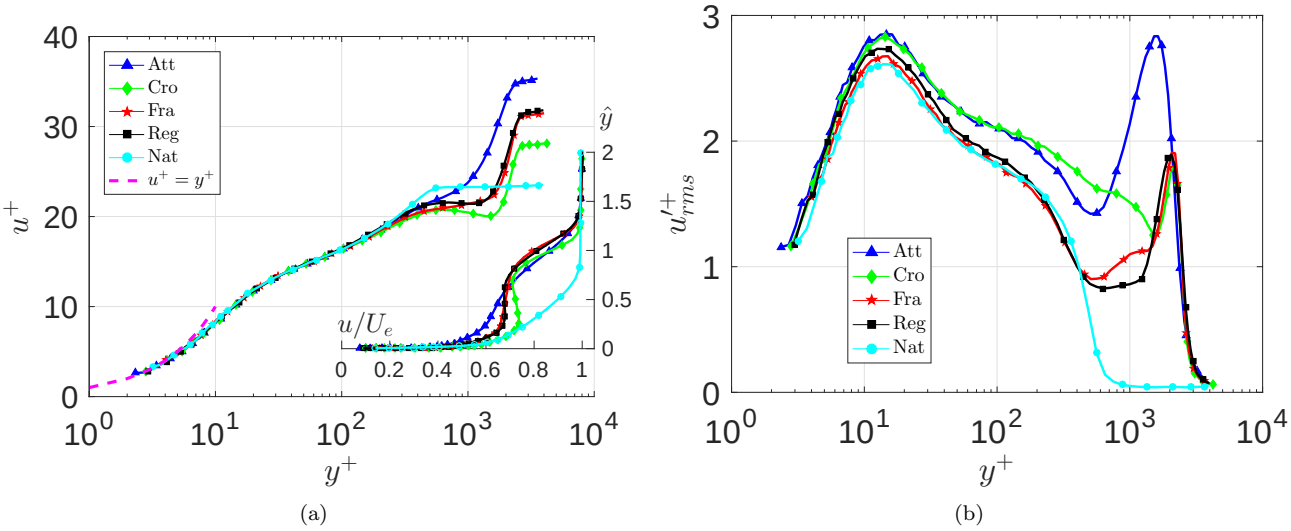

Figure 7: (a) Mean velocity profile for various grids at $\hat{x} = 9$ in inner (main figure) and outer scaling (inset). N.B. In the natural case $h = 0$ so we define $\hat{y} = y/\delta$. (b) rms profile for various grids at $\hat{x} = 9$ in inner scaling.

Before showing results of $\tau'^{+}_{w,rms}$, let us analyse the u'^{+}_{rms} profile at $\hat{x} = 9$ acquired with the FHW (figure 7(b)). Two different trends can be observed; first *Fra* and *Reg* cases present a value of u'^{+}_{rms} collapsing perfectly with the natural case for $y^+ < 400$, i.e. the inner and logarithmic layers. A larger turbulent activity is presented at $\hat{y} \approx 1 \rightarrow y^+ \approx 2000$ corresponding with the shear layer formed above the porous fence. These two regions seem to have little interaction contrasting with the *Att* and *Cro* cases where the large turbulent intensity of the outer region propagates into the near wall region increasing the value of u'^{+}_{rms} for $15 \leq y^+ \leq 300$ above the expected value for the natural case; this is also confirmed by spectral content, not shown for brevity. Note that, in general, the inner and logarithmic regions of the flow present a very clear inner scaling in the mean profile (figure 7(a)) but not so clear for the rms profile (figure 7(b)) due to the large influence of the highly-turbulent outer flow. Analogously, the mean wall shear stress $\overline{\tau_w}$ seems to present a better recovery than its rms level as will be shown below.

Regarding the behaviour at the wall, figure 8(a) shows the value of $\tau'^{+}_{w,rms}$ as a function of Re_τ. Following the methodology explained in 3.2, fluctuating wall shear stress is measured with WHW sensor and then corrected with equation 3. As opposed to the natural case (where δ was obtained by a fitting to the velocity profile), Re_τ will be based on δ_{99} due to the difficulty of an adequate fitting of a wake description to the mean velocity profile (see figure 7). For natural TBL one can assume with good accuracy $\delta \simeq 1.3\delta_{99}$; furthermore, there is only a weak logarithmic dependence of $\tau'^{+}_{w,rms}$ on Re_τ, hence, the selection of δ_{99} as TBL edge is sufficient for

this purpose.

Solid lines link the different points in increasing order of $\hat{x}$; however, the evolution of Re_τ with the streamwise coordinate is not uniform. This fact is mainly due to the non-uniform trend followed by u_τ; but also because δ_{99} is not monotonously increasing due to the interaction of the wakes of different bars in the near field. These facts make it difficult to extrapolate any clear trend in the vicinity of the grids. Moreover, different grids may generate distinct turbulent structures which may influence the near wall region differently (Rodríguez-López et al., 2016b). Further downstream, the boundary layer growth appears to be uniform and more solid conclusions can be drawn. At the furthest measurement station, *Fra* and *Reg* grids present a value of $\tau^{\prime+}_{w,rms}$ within 1% of that expected for a natural TBL at that Re_τ. Slightly larger deviation (2%) is encountered for the *Cro* case but still this is roughly the same dispersion encountered in the natural case employed for validation. This result contrasts with the that for the *Att* grid in which the fluctuations are approximately 10% higher than a natural TBL. This deviation is larger than the uncertainty and should not be wrongly attributed to a measurement error (since uncertainty is $\mathcal{O}(2\%)$). This result contrasts with the previous section 4.1 which showed that the mean u_τ was not affected by the presence of the grids. It is reasonable to conclude that this may be due to the larger influence of the outer (highly turbulent) fluid in the inner region (shown also in figure 7(b)). However, in order to study this effect more deeply for the *Att* case the probability density function will be considered.

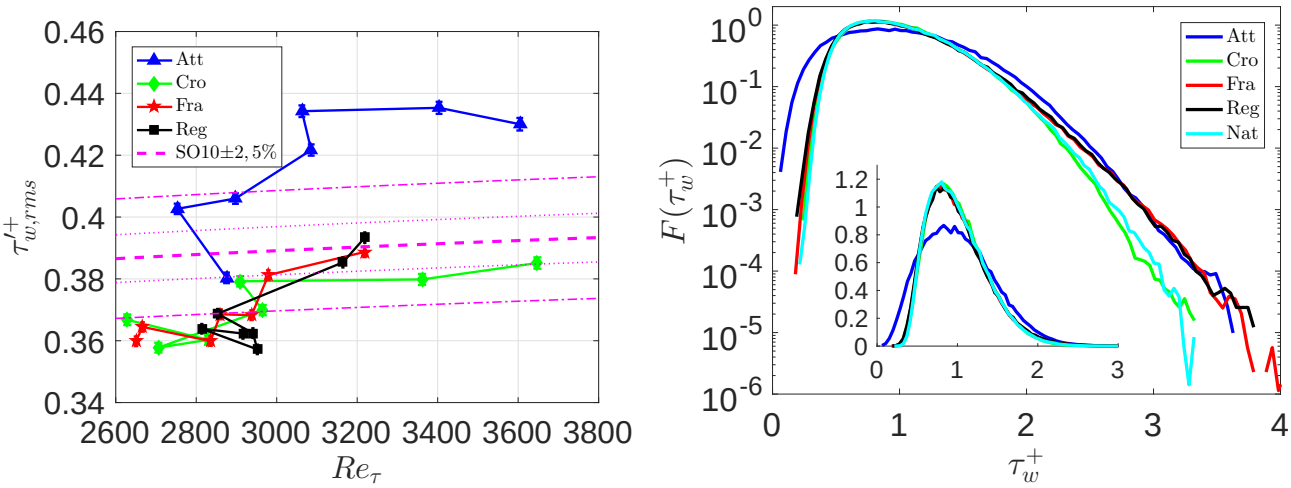

Figure 8: (a) Value of the rms of the fluctuations of wall shear stress for various grids. Dashed pink line —SO10— shows the correlation $\tau^{\prime+}_{w,rms} = 0.245 + 0.018\log(Re_\tau)$ (Schlatter and Örlü, 2010a) with ±2% (dotted) and ±5% (dot-dashed) margins. (b) Probability density function, $F(\tau_w^+)$, for various grids at equivalent $Re_\tau \approx 3300$ except for natural case ($Re_\tau = 1530$ is the largest available). Inset shows the same data in linear scale.

Section 3.2 has shown the trend followed by the probability density function with Re; in order to provide a fair comparison between the various grids, a similar Reynolds number should be chosen. Results are presented in figure 8(b) for $Re_\tau \approx 3300$; this is selected as a compromise between keeping the largest possible distance to the grid and the availability for all the cases. The natural case (with $Re_\tau = 1530$) is also shown for reference. Note that, as shown in section 3.2, the Reynolds number effect is expected to be confined to extreme values of τ_w^+. Figure 8(b) shows a clear departure from the expected trend for the *Att* case, which exhibits a less skewed distribution ($S \approx 0.51$ as opposed to $S \approx 0.8$ for the *Fra* and *Reg* cases) and a smaller flatness factor ($K \approx 3$ as opposed to $K \approx 4$ for *Fra* and *Reg* cases). This supports the aforementioned hypothesis in which the outer fluid (with negative or zero skewness, see, for instance Alfredsson et al. 2011 or Schlatter and Örlü 2010b) is influencing the near wall region (characterized by a large positive S) causing a departure from its expected form. PDF in figure 8(b) also highlights the presence of a smaller tail than expected for the *Cro* case, probably accounting for the slightly small value of $\tau^{\prime+}_{w,rms}$ in figure 8(a) for $Re_\tau \approx 3600$.

4.3 Spectra $fE_{11}(\tau_w^+)$ and autocorrelation.

Two conclusions can be drawn at this point regarding the shear stress in the grid+TBL configuration: (i) within experimental uncertainty the mean value seems to be unaffected by the presence of the porous fences and (ii) the fluctuating value seems to be coherent with the natural ZPG TBL case except in the *Att* case where an enhanced influence of the highly turbulent outer fluid on the inner region makes it ≈ 10% larger than the expected value. Further insight into these effects is sought with analysis of the spectral content and the autocorrelation of τ_w.

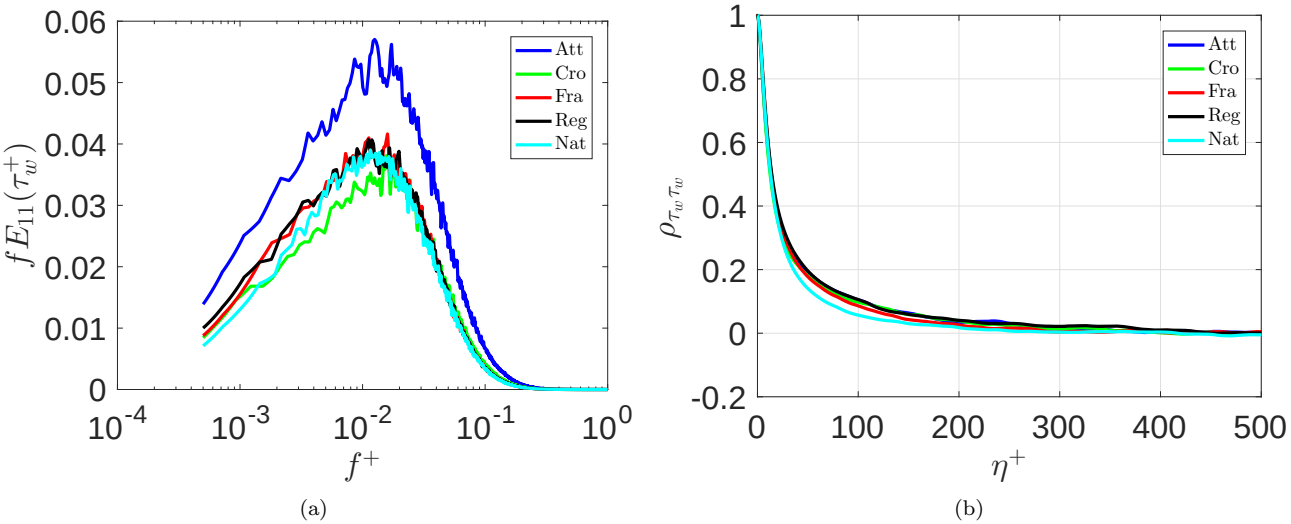

(a) (b)

Figure 9: (a) Pre-multiplied power spectral density, $fE_{11}(\tau_w^+)$; for various grids at equivalent $Re_\tau \approx 3300$, natural case $Re_\tau = 1530$. (b) Autocorrelation of wall shear stress, $\rho_{\tau_w\tau_w}$, as a function of the time lag scaled in inner units $\eta^+ = \eta u_\tau^2/\nu$.

Pre-multiplied spectral content at $Re_\tau \approx 3300$ (same data of figure 8(b)) is shown in figure 9(a). The smaller value of $\tau'^+_{w,rms}$ for the *Cro* case may be related to a slightly lower energy at medium frequencies $f^+ = f\nu/u_\tau^2 \approx \mathcal{O}(0.005)$. One possible explanation could be the large number of squares of this grid; which might be highly effective in breaking down the fluid structures hence making it more difficult to generate large eddies. From a totally different perspective (opposed jet combustion), Goh et al. (2014) showed that this configuration (fractal grids based on cross pattern) is significantly effective at reducing the influence of upstream conditions by breaking down fluid structures in the subsequent flow field.

Regarding the *Att* case, it has been suggested that it presents a larger influence of the outer (bigger) fluid structures into the near wall region. However, the pre-multiplied spectrum does not show any preferential frequency, the spectral level is uniformly larger for every f^+. A possible explanation could be related to the large number of wakes generated by the numerous bars of different sizes that this geometry presents close to the wall ($\hat{y} < 0.3$, figure 2.3). These wakes generate a highly turbulent fluid which would undoubtedly improve the mixing of the outer and inner regions thus potentially increasing the fluctuating level in the inner region; a similar effect has been reported for over-tripped boundary layers downstream of blunt obstacles generating large recirculation regions (Rodríguez-López et al., 2016b). Another possible explanation could be that the outer, highly energetic, fluid is seen as a different boundary condition for the inner region which, contrary to the natural case, enhances the level of the fluctuations of the near-wall region without changing its characteristic frequency. This mechanism could be explained in a similar manner to outer-inner modulation (Mathis et al., 2009; Marusic et al., 2010a; Chernyshenko et al., 2012) where the outer fluid (more energetic, with a greater length-scale) acts as a quasi-steady boundary condition for the inner cycle which increases its intensity.

Study of the autocorrelation factor can provide an estimation of the typical time-scale in the inner region. Considering a certain time lag expressed in inner units, η^+, the correlation factor can be defined as:

$$\rho_{\tau_w\tau_w}(\eta^+) = \frac{\overline{\tau'_w(t^+) \cdot \tau'_w(t^+ + \eta^+)}}{\tau'^2_{rms}} \tag{4}$$

where the overline represents the time average. Figure 9(b) shows a slight difference between the $Re_\tau \approx 1500$ natural case to the grid+TBL cases which all have $Re_\tau \approx 3300$. Other than this, the different grids do not have a very large effect on the autocorrelation (as can be inferred by the location of the spectral peak in figure 9(a)). Furthermore, correlation is lost after approximately 200 time units, similar to average streak persistence reported by Smith and Metzler (1983). If we assume a convection velocity for the shear stress fluctuations of $\mathcal{O}(10u_\tau)$ (Jeon et al., 1999), this would be equivalent to a characteristic length of $\mathcal{O}(1000\delta_\nu)$, broadly reported as characteristic of the inner cycle (e.g. Marusic et al., 2010b, amongst others). However, no changes are seen for the different grids, this suggests that (even for the *Att* case) the turbulent mechanisms in the near-wall region remain relatively unaltered in time and length scales even though they may have a larger intensity (such as the *Att* case, well illustrated in figures 8(a) and 9(a)) as a consequence of the interaction of the outer fluid in the inner region.

Summarizing, *Fra* and *Reg* grids seem to produce a TBL in the far field which reproduces the inner behaviour of an equivalent *Re* ZPG TBL. On the other hand, probability density function of the fluctuations for the most

disrupted case (*Att*) suggest that there is an enhanced influence of the grid's wake in the near-wall region (which diminishes skewness and kurtosis factors). As a consequence of this interaction the value of $\tau'^{+}_{w,rms}$ is up to 10% larger than the expected value. However, due to the dominant constraint imposed by the wall, near-wall mechanisms seem to remain unaltered (both in frequency and correlation length) despite their larger rms level (a good collapse in inner variables is also obtained for the mean and rms velocity profiles). *Cro* grid seems to break-up large turbulent structures more effectively as evidenced by a reduction of relatively large ($f^+ \approx 0.005$) structures and a decrease of the positive extreme events of shear stress (right tail figure 8(b)).

5 Conclusions

Mean and fluctuating values of wall shear stress have been measured in the flow downstream of low porosity single-and multi-scale wall-mounted fences. Special attention has been paid to a prior validation of the measurement technique (wall-mounted hot wire, WHW) applied to a naturally growing ZPG TBL. Such flows have been extensively studied meaning that their properties are canonical. We are thus able to obtain an expected degree of uncertainty for this measurement technique when applied to the substantially disrupted cases.

Four different extrapolation methods for u_τ (from the velocity profile) have been tested showing that, in general, their uncertainty can be kept $\mathcal{O}(1\%)$ for natural ZPG TBL. In particular the method proposed by Alfredsson et al. (2011) has been applied to real data enabling a similar uncertainty after a careful selection of the parameters involved. Moreover, further modification to extract u_τ is proposed from the method of Vinuesa and Nagib (2016) showing an excellent agreement with other extrapolation methods. Regarding the direct measurement of τ_w using a wall hot wire (WHW); it presents a large uncertainty in the determination of the mean value ($\mathcal{O}(4\%)$ with a tendency to the overestimation). However, rms level of the fluctuations is correctly measured (after applying the corrections proposed by (Smits et al., 2011) and (Miller et al., 2014)) to within 2% or better of the value suggested by Schlatter and Örlü (2010a).

With the accuracy of the methodology established, results are presented using four different single- and multi-scale wall-mounted grids. There is evidence showing that all of them maintain the same turbulent structures and mechanisms in the near-wall region (at least when sufficiently far downstream of the grids). This is in agreement with previous studies showing the quicker recovery from disrupted conditions in the near-wall region as opposed to a slow adaptation of the outer fluid. Of the grids tested, *Cro* and *Att* cases most strongly disrupt the wall shear stress behaviour producing a reduction and increase of its fluctuating level respectively. While the former may be explained by a more effective destruction of large-scale turbulent structures, the latter suggests (because of its smaller skeweness and kurtosis) a larger influence of the grid's wake on the near-wall region. However, as mentioned, all the results seem to point towards a rapid recovery of the canonical ZPG TBL turbulent mechanisms downstream of the four employed wall-mounted porous fences.

Acknowledgments

The authors would like to acknowledge the financial support given by European Union FP7 Marie Curie MULTISOLVE project (Grant agreement No. 317269).

References

H. Schlichting and K. Gersten. *Boundary Layer Theory*. Springer, 8th edition, 2000. ISBN 3-540-66270-7.

C. Tropea and A. Yarin. *Springer handbook of experimental fluid mechanics*. Springer, Berlin, 2007.

H. M. Nagib, C. Christophoro, J. D. Reudi, P. A. Monkewitz, and S. Gravante. Can We Ever Rely on Results from Wall-Bounded Turbulent Flows without Direct Measurements of Wall Shear Stress? In *Aerodynamic Measurement Technology and Ground Testing Conference*, pages 1–12, Portland, Oregon, 2004.

H. M. Nagib, K. A. Chauhan, and P. A. Monkewitz. Approach to an asymptotic state for zero pressure gradient turbulent boundary layers. *Philosophical transactions. Series A, Mathematical, physical, and engineering sciences*, 365:755–770, 2007. doi: 10.1098/rsta.2006.1948.

K. A. Chauhan, P. A. Monkewitz, and H. M. Nagib. Criteria for assessing experiments in zero pressure gradient boundary layers. *Fluid Dynamics Research*, 41(2):021404, 2009. doi: 10.1088/0169-5983/41/2/021404.

P. Schlatter and R. Örlü. Assessment of direct numerical simulation data of turbulent boundary layers. *Journal of Fluid Mechanics*, 659:116–126, 2010a. doi: 10.1017/S0022112010003113.

P. H. Alfredsson, R. Örlü, and P. Schlatter. The viscous sublayer revisited – exploiting self-similarity to determine the wall position and friction velocity. *Experiments in Fluids*, 51(1):271–280, 2011. doi: 10.1007/s00348-011-1048-8.

Z. Hu, C. L. Morfey, and N. D. Sandham. Wall Pressure and Shear Stress Spectra from Direct Simulations of Channel Flow. *AIAA Journal*, 44(7):1541–1549, 2006. doi: 10.2514/1.17638.

R. Örlü and P. Schlatter. On the fluctuating wall-shear stress in zero pressure-gradient turbulent boundary layer flows. *Physics of Fluids*, 23(2), 2011. doi: 10.1063/1.3555191.

S. Jeon, H. Choi, J. Y. Yoo, and P. Moin. Space–time characteristics of the wall shear-stress fluctuations in a low-Reynolds-number channel flow. *Physics of Fluids*, 11(10):3084, 1999. doi: 10.1063/1.870166.

I. Marusic, K. A. Chauhan, V. Kulandaivelu, and N. Hutchins. Evolution of zero-pressure-gradient boundary layers from different tripping conditions. *Journal of Fluid Mechanics*, 783:379–411, 2015. doi: 10.1017/jfm.2015.556.

E. Rodríguez-López, P. J. K. Bruce, and O. R. H. Buxton. On the Formation Mechanisms of Artificially Generated High Reynolds Number Turbulent Boundary Layers. *Boundary-Layer Meteorology*, 160(2):201–224, 2016a. doi: 10.1007/s10546-016-0139-8.

M. P. Simens, J. Jimenez, S. Hoyas, and Y. Mizuno. A high-resolution code for turbulent boundary layers. *Journal of Computational Physics*, 228(11):4218–4231, 2009. doi: 10.1016/j.jcp.2009.02.031.

F. H. Clauser. Turbulent Boundary Laers in Adverse Pressure Gradients. *Journal of Aeronautical Sciences*, 21 (2):91–108, 1954.

A. Kendall and M. Koochesfahani. A method for estimating wall friction in turbulent wall-bounded flows. *Experiments in Fluids*, 44(5):773–780, 2008. doi: 10.1007/s00348-007-0433-9.

E. Rodríguez-López, P. J. K. Bruce, and O. R. H. Buxton. A robust post-processing method to determine skin friction in turbulent boundary layers from the velocity profile. *Experiments in Fluids*, 56(4):68, 2015. doi: 10.1007/s00348-015-1935-5.

R. Vinuesa and H. M. Nagib. Enhancing the accuracy of measurement techniques in high Reynolds number turbulent boundary layers for more representative comparison to their canonical representations. *European Journal of Mechanics, B/Fluids*, 55(2):300–312, 2016. doi: 10.1016/j.euromechflu.2015.09.004.

P. H. Alfredsson, A. V. Johansson, J. H. Haritonidis, and H. Eckelmann. The fluctuating wall-shear stress and the velocity field in the viscous sublayer. *Physics of Fluids*, 31(5):1026, 1988. doi: 10.1063/1.866783.

D. Hurst and J. C. Vassilicos. Scalings and decay of fractal-generated turbulence. *Physics of Fluids*, 19(3): 035103, 2007. doi: 10.1063/1.2676448.

S. Laizet and J. C. Vassilicos. Multiscale generation of turbulence. *Journal of Multiscale Modelling*, 1(1): 177–196, 2009.

N. Mazellier and J. C. Vassilicos. Turbulence without Richardson-Kolmogorov cascade. *Phys. Fluids*, 22(7): 075101, 2010.

H. Suzuki, K. Nagata, Y. Sakai, and R. Ukai. High-Schmidt-number scalar transfer in regular and fractal grid turbulence. *Physica Scripta*, dec 2010. doi: 10.1088/0031-8949/2010/T142/014069.

P. C. Valente and J. C. Vassilicos. The decay of turbulence generated by a class of multiscale grids. *Journal of Fluid Mechanics*, 687:300–340, 2011. doi: 10.1017/jfm.2011.353.

P. C. Valente and J. C. Vassilicos. Universal Dissipation Scaling for Nonequilibrium Turbulence. *Physical Review Letters*, 108(21):214503, 2012. doi: 10.1103/PhysRevLett.108.214503.

R. Gomes-Fernandes, B. Ganapathisubramani, and J. C. Vassilicos. Particle image velocimetry study of fractal-generated turbulence. *Journal of Fluid Mechanics*, 711:306–336, 2012. doi: 10.1017/jfm.2012.394.

S. Discetti, I. B. Ziskin, T. Astarita, R. J. Adrian, and K. P. Prestridge. PIV measurements of anisotropy and inhomogeneity in decaying fractal generated turbulence. *Fluid Dynamics Research*, 45(6):061401, 2013.

J. Nedić, B. Ganapathisubramani, J. C. Vassilicos, J. Borée, L. E. Brizzi, and A. Spohn. Aeroacoustic Performance of Fractal Spoilers. *AIAA Journal*, 50(12):2695–2710, 2012. doi: 10.2514/1.J051387.

J. Nedić, J. C. Vassilicos, and B. Ganapathisubramani. Axisymmetric Turbulent Wakes with New Nonequilibrium Similarity Scalings. *Physical Review Letters*, 111, 2013. doi: 10.1103/PhysRevLett.111.144503.

T. Dairay, M. Obligado, and J. C. Vassilicos. Non-equilibrium scaling laws in axisymmetric turbulent wakes. *J. Fluid Mech.*, 781(1989):166–195, 2015. doi: 10.1017/jfm.2015.493.

J. Nedić and J. C. Vassilicos. Vortex shedding and aerodynamic performance of an airfoil with multi-scale trailing edge modifications. *AIAA Journal*, 53(11):1–24, 2015. doi: 10.2514/1.J053834.

K. H. H. Goh, P. Geipel, F. Hampp, and R. P. Lindstedt. Flames in fractal grid generated turbulence. *Fluid Dynamics Research*, 45(6):061403, 2013. doi: 10.1088/0169-5983/45/6/061403.

K.H.H. Goh, P. Geipel, and R.P. Lindstedt. Lean premixed opposed jet flames in fractal grid generated multiscale turbulence. *Combustion and Flame*, 2014. doi: 10.1016/j.combustflame.2014.03.010.

J. Nedić, O. Supponen, B. Ganapathisubramani, and J. C. Vassilicos. Geometrical influence on vortex shedding in turbulent axisymmetric wakes. *Physics of Fluids*, 27(3), 2015. doi: 10.1063/1.4913573.

G. Melina, P. J. K. Bruce, and J. C. Vassilicos. Vortex shedding effects in grid-generated turbulence. *Physical Review Fluids*, 1(4):044402, 2016. doi: 10.1103/PhysRevFluids.1.044402.

C. J. Keylock, K. Nishimura, M. Nemoto, and Y. Ito. The flow structure in the wake of a fractal fence and the absence of an inertial regime. *Environmental Fluid Mechanics*, 12(3):227–250, 2012. doi: 10.1007/s10652-011-9233-0.

Philipp Schlatter and Ramis Örlü. Turbulent boundary layers at moderate Reynolds numbers: inflow length and tripping effects. *Journal of Fluid Mechanics*, 710:5–34, 2012. ISSN 0022-1120.

E. Rodríguez-López, P. J. K. Bruce, and O. R. H. Buxton. Near field development of artificially generated high Reynolds number turbulent boundary layers. *Physical Review Fluids (*In press*)*, (-):–, 2016b.

P. C. Valente and J. C. Vassilicos. The non-equilibrium region of grid-generated decaying turbulence. *Journal of Fluid Mechanics*, 744:8–37, 2014.

Marcus Hultmark, Anand Ashok, and Alexander J Smits. A new criterion for end-conduction effects in hot-wire anemometry. *Measurement Science and Technology*, 22(5):055401, 2011.

M.A. Miller, B Estejab, and S. C. C. Bailey. Evaluation of hot-wire spatial filtering corrections for wall turbulence and correction for end-conduction effects. *Experiments in Fluids*, 55(5):1735, 2014.

Peter Lenaers, Qiang Li, Geert Brethouwer, Philipp Schlatter, and Ramis Örlü. Rare backflow and extreme wall-normal velocity fluctuations in near-wall turbulence. *Physics of Fluids*, 24(3):035110, 2012.

A.A. Townsend. *The Structure of Turbulent Shear Flow*. Cambridge university Press, Cambridge and New York, 2 edition, 1976.

S. Laizet and J. C. Vassilicos. Fractal space-scale unfolding mechanism for energy-efficient turbulent mixing. *Physical review. E, Statistical, nonlinear, and soft matter physics*, 86(4 Pt 2):046302, 2012.

A.J. Musker. Explicit Expression for the Smooth Wall Velocity Distribution in a Turbulent Boundary Layer. *AIAA Journal*, pages 655–657, 1979.

H. M. Nagib and K. A. Chauhan. Variations of von Karman coefficient in canonical flows. *Physics of Fluids*, 20(10):101518, 2008. doi: 10.1063/1.3006423.

A. J. Smits, J. P. Monty, M. Hultmark, S. C. C. Bailey, N. Hutchins, and I. Marusic. Spatial resolution correction for wall-bounded turbulence measurements. *Journal of Fluid Mechanics*, 676(2011):41–53, 2011. doi: 10.1017/jfm.2011.19.

A. Segalini, A. Cimarelli, J.-D. Rüedi, E. De Angelis, and A. Talamelli. Effect of the spatial filtering and alignment error of hot-wire probes in a wall-bounded turbulent flow. *Meas. Sci. Tech. (submitted)*, 22(10): 105408, 2010. doi: 10.1088/0957-0233/22/10/105408.

A. Talamelli, A. Segalini, R. Örlü, P. Schlatter, and P. H. Alfredsson. Correcting hot-wire spatial resolution effects in third- and fourth-order velocity moments in wall-bounded turbulence. *Experiments in Fluids*, 54 (4):1496, 2013. doi: 10.1007/s00348-013-1496-4.

R.M. Fand. Heat transfer by forced convection from a cylinder to water in crossflow. *International Journal of Heat and Mass transfer*, 8(7):995–1010, 1965.

L. V. Krishnamoorthy, D. H. Wood, R. A. Antonia, and A. J. Chambers. Effect of wire diameter and overheat ration near a conducting wall. *Experiments in Fluids*, 3:121–127, 1985.

Y. T. Chew, B. C. Khoo, and G. L. Li. An investigation of wall effects on hot-wire measurements using a bent sublayer probe. *Measurement Science and Technology*, 9:67–85, 1998.

N. Hutchins and K.-S. Choi. Accurate measurements of local skin friction coefficient using hot-wire anemometry. *Progress in Aerospace Sciences*, 38:421–446, 2002. doi: 10.1016/S0376-0421(02)00027-1.

P. H. Alfredsson and R. Örlü. The diagnostic plot – a litmus test for wall bounded turbulence data. *European Journal of Mechanics - B/Fluids*, 29(6):403–406, 2010. doi: 10.1016/j.euromechflu.2010.07.006.

R. Mathis, N. Hutchins, and I. Marusic. Large-scale amplitude modulation of the small-scale structures in turbulent boundary layers. *Journal of Fluid Mechanics*, 628:311–337, 2009. doi: 10.1017/S0022112009006946.

I. Marusic, R. Mathis, and N. Hutchins. Predictive model for wall-bounded turbulent flow. *Science (New York, N.Y.)*, 329(5988):193–196, 2010a. doi: 10.1126/science.1188765.

S. I. Chernyshenko, I. Marusic, and R. Mathis. Quasi-steady description of modulation effects in wall turbulence. *arXiv:1203.3714v1 [physics.flu-dyn]*, page 16, 2012.

P. Schlatter and R. Örlü. Quantifying the interaction between large and small scales in wall-bounded turbulent flows: A note of caution. *Physics of Fluids*, 22(5):051704, 2010b. doi: 10.1063/1.3432488.

C.R. Smith and S.P. Metzler. Characterization of low-speed streaks in the near-wall region of a turbulent boundary layer. *Journal of Fluid Mechanics*, 129:27–54, 1983. doi: 10.1016/j.euromechflu.2003.12.005.

I. Marusic, B. J. McKeon, P. A. Monkewitz, H. M. Nagib, A. J. Smits, and K. R. Sreenivasan. Wall-bounded turbulent flows at high Reynolds numbers: Recent advances and key issues. *Physics of Fluids*, 22(6), 2010b. doi: 10.1063/1.3453711.